

Sabatier Phenomenon in Hydrogenation Reactions Induced by Single-Atom Density

Hongqiang Jin,[#] Runqing Zhao,[#] Peixin Cui, Xiaolong Liu, Jie Yan, Xiaohu Yu,* Ding Ma,* Weiguo Song, and Changyan Cao*



Cite This: *J. Am. Chem. Soc.* 2023, 145, 12023–12032



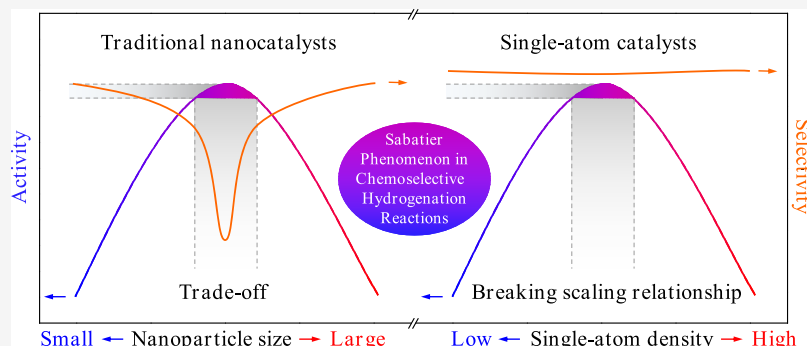
Read Online

ACCESS |

Metrics & More

Article Recommendations

Supporting Information



ABSTRACT: The Sabatier principle is a fundamental concept in heterogeneous catalysis that provides guidance for designing optimal catalysts with the highest activities. For the first time, we here report a new Sabatier phenomenon in hydrogenation reactions induced by single-atom density at the atomic scale. We produce a series of Ir single-atom catalysts (SACs) with a predominantly $\text{Ir}_1\text{-P}_4$ coordination structure with densities ranging from 0.1 to 1.7 atoms/ nm^2 through a P-coordination strategy. When used as the catalysts for hydrogenation, a volcano-type relationship between Ir single-atom density and hydrogenation activity emerges, with a summit at a moderate density of 0.7 atoms/ nm^2 . Mechanistic studies show that the balance between adsorption and desorption strength of the activated H^* on Ir single atoms is found to be a key factor for the Sabatier phenomenon. The transferred Bader charge on these Ir SACs is proposed as a descriptor to interpret the structure–activity relationship. In addition, the maximum activity and selectivity can be simultaneously achieved in chemoselective hydrogenation reactions with the optimized catalyst due to the uniform geometric and electronic structures of single sites in SACs. The present study reveals the Sabatier principle as an insightful guidance for the rational design of more efficient and practicable SACs for hydrogenation reactions.

INTRODUCTION

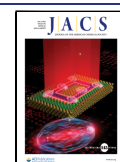
The Sabatier principle is a fundamental concept in heterogeneous catalysis that guides the design of optimal catalysts with the highest activities.^{1–3} It states that the best catalysts should have proper binding strength for key reactive intermediates: neither too strong, which results in high coverage and surface poisoning, nor too weak, which leads to disfavored activation.^{4–7} In both cases, the reaction rates are hampered. Experimentally, this principle is readily illustrated in a so-called volcano plot, in which the top of the volcano represents the maximum activity.^{8–10} However, because of the scaling relationship, increased activity frequently accompanies decreased selectivity in selective catalytic reactions.^{6,11–13} Numerous studies have demonstrated that the catalytic performances of noble metal catalysts are indeed restricted by the scaling relationship, which normally results in a trade-off between activity and selectivity and thus limits the optimization of the overall catalytic performance in the case of chemoselective hydrogenation reactions, one of the most

useful reactions in the chemical industry.^{11,12,14} Therefore, developing a strategy that can break the scaling relationship and achieve the highest activity and selectivity simultaneously is highly desirable.

It has been consented that selectivity is largely determined by the adsorption strength and configuration of reactants/intermediates on the surface of catalysts, which in turn is governed by the electronic and geometric structures of the active sites.^{15–17} Therefore, to achieve high chemoselectivity, the catalytic active sites should have uniform geometric and electronic structure that allow only the target functional group to be adsorbed via a specific manner on the catalyst.^{18,19} In this

Received: January 20, 2023

Published: May 26, 2023



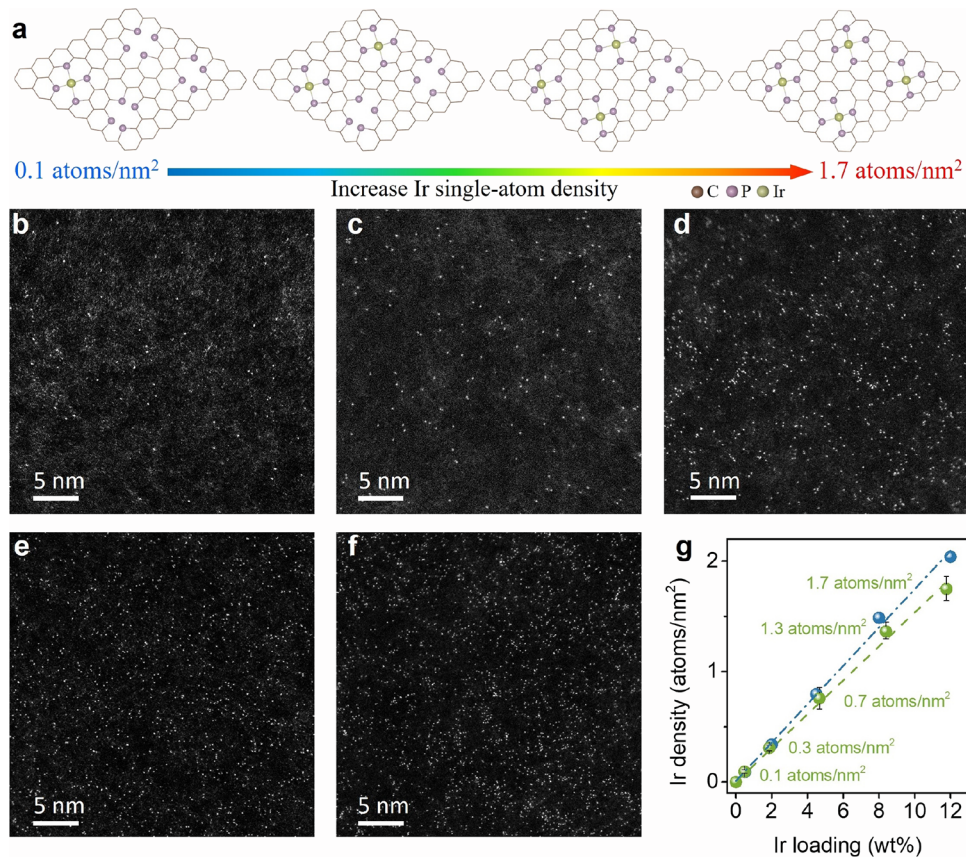


Figure 1. Synthesis and characterization of Ir SACs with different loadings. (a) Schematic illustration of Ir SACs with varying density. (b–f) AC HAADF-STEM images of various samples with different metal loadings of 0.5 wt % (b), 2 wt % (c), 4.5 wt % (d), 8 wt % (e), and 12 wt % (f). (g) Plot of Ir surface density (atoms/nm^2) measured with the statistical method (green dots) from five independent STEM images and calculated with BET surface area (blue dots) against the corresponding Ir loadings. Error bars correspond to the standard deviations of Ir density for each sample in five independent areas.

regard, single-atom catalysts (SACs) with the unique geometric and electronic structures typically exhibit impressive selectivity in chemoselective hydrogenation reactions, providing an ideal solution to the activity–selectivity trade-off.^{19–22} Furthermore, SACs have the advantage of maximizing the utilization of metal atoms to reduce costs, especially for noble metal catalysts.^{23–25} Therefore, we can still follow the Sabatier principle to screen the optimal SACs with the maximum activity while maintaining high selectivity to break the scaling relationship. However, to the best of our knowledge, the Sabatier phenomenon in hydrogenation reactions at the single atomic scale has not been reported.

In this work, we report such a Sabatier phenomenon induced by single-atom density. We first produced a series of Ir SACs with different densities ranging from 0.1 to 1.7 atoms/ nm^2 through a P-coordination strategy. Aberration-corrected high angle annular dark-field scanning transmission electron microscopy (AC HAADF-STEM) and X-ray absorption fine structure (XAFS) characterizations confirmed that all the obtained Ir SACs were atomically dispersed with a predominantly $\text{Ir}_1\text{-P}_4$ coordination structure. However, the valence states of Ir species shift downward to metallic with increasing densities, indicating that the electronic structures of Ir single atoms were altered, which was attributed to the interaction among the single sites in densely packed SACs. When used for hydrogenation reactions, volcano curves were observed between Ir single-atom density and hydrogenation

activity, with a summit at a moderate density of 0.7 atoms/ nm^2 . Further mechanism studies disclose that the adsorption and desorption strength of the activated H^* atoms on Ir single atoms is found to be a key factor for the Sabatier phenomenon. The transferred Bader charge on these Ir SACs was proposed as a descriptor to interpret the structure–activity relationship. Furthermore, due to the uniform geometric and electronic structures of single sites in SACs, the maximum activity and selectivity can be simultaneously achieved in chemoselective hydrogenation reactions with the optimized catalyst. This work reveals the Sabatier phenomenon at the single atomic scale and highlights the significance of SAC-density effect on hydrogenation reactions, providing insightful guidance for rational design of more efficient and practicable SACs.

RESULTS AND DISCUSSION

Synthesis and Characterizations of Ir SACs with Various Densities. Ir SACs with a specific $\text{Ir}_1\text{-P}_4$ coordination structure were synthesized through the traditional pyrolysis strategy with addition of phytic acid as a phosphorus source for anchoring sites (detail procedures are shown in Experimental Section). By adjusting the amounts of metal precursor iridium(III) chloride (IrCl_3), Ir SACs with mass loadings ranging from ~0.5 to 12 wt % can be obtained as determined by inductively coupled plasma atomic emission spectrometry (ICP-AES) (Figure 1a and Table S1). The absence of diffraction peaks associated with Ir crystal in their X-ray

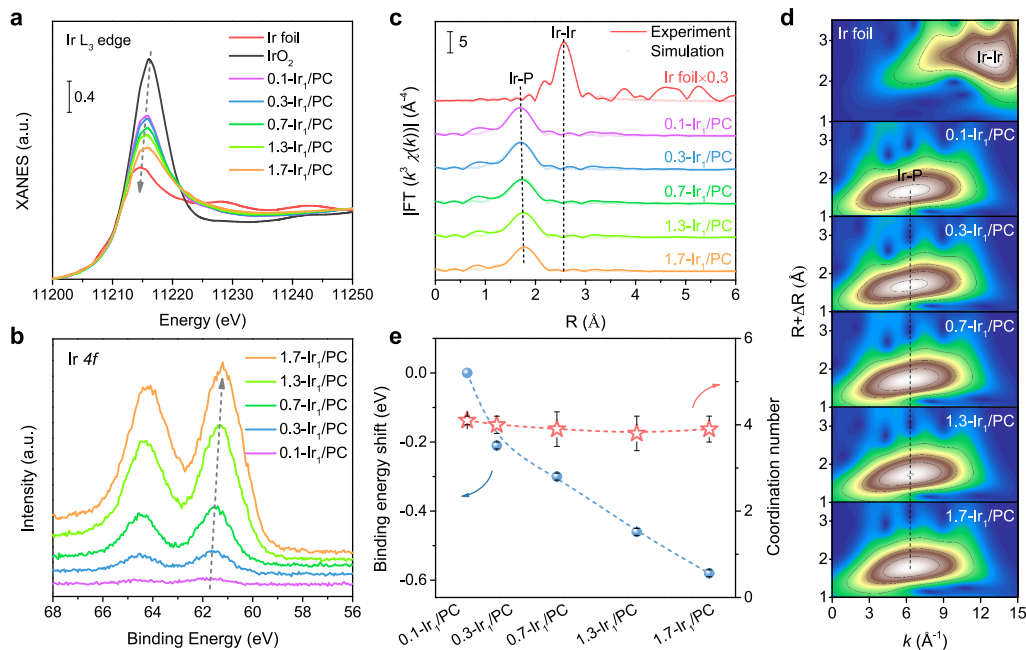


Figure 2. Atomic structural analysis and electronic property of the Ir SACs. (a) Ir L₃-edge XANES spectra of x -Ir₁/PC, Ir foil, and IrO₂ samples. (b) Ir 4f_{7/2} XPS spectra of x -Ir₁/PC samples. (c) Fourier-transformed k^3 -weighted EXAFS spectra of x -Ir₁/PC and references. (d) Wavelet transform analysis of x -Ir₁/PC samples. (e) Ir 4f_{7/2} binding energy shift and coordination numbers of x -Ir₁/PC samples with respect to Ir density.

diffraction (XRD) patterns indicates that Ir species in all above samples are highly dispersed (Figure S1). Further increasing Ir loading to 16 wt % will result in the appearance of Ir clusters (Figure S2). Typical scanning electron microscopy (SEM) and transmission electron microscopy (TEM) images show that all the obtained samples are composed of two-dimensional thin nanosheet structures (Figures S3 and S4). No metal clusters or nanoparticles were observed in their high-resolution TEM images. The corresponding energy-dispersive spectroscopy (EDS) mapping images show that Ir elements are uniformly distributed over the P-doped carbon support (Figure S5), suggesting the highly dispersed Ir species in these samples even for Ir loading as high as 12 wt %, which agrees well with XRD results. AC HAADF-STEM was then performed to confirm the atomic dispersion of Ir species. As shown in Figure 1b–f, the bright dots can be identified as Ir single atoms due to the heavy Z-contrast. It can be intuitively seen that the surface Ir density gradually increases with the increase in Ir loadings, probably producing a lot of adjacent single atoms at high Ir density (Figure S6).

Realizing the uniform dispersion of Ir single atoms over a broad loading permits the convincing analysis of the surface density at desirable locations. The measured Brunauer–Emmett–Teller (BET) specific surface areas of these Ir SACs all exceeded 1000 m²·g⁻¹, which ensured that Ir atoms can be anchored and exposed on the surface (Figure S7). Considering that Ir atoms were dispersed in the two-dimensional thin nanosheets, we first used the statistical method to determine the surface density of Ir single atoms based on the AC HAADF-STEM images, which is one of the most effective experimental methods in the literature for estimating the single-atom density or inter-site distance.^{26–29} Bright spots with nearly the same brightness in five independent AC HAADF-STEM images at specified areas were taken into consideration for each sample (Figure 1b–f and Figures S8–S12), where all Ir atoms were able to be

counted (Figure S13). As shown in Figure 1g, the statistical density of Ir SACs is in the range of 0.1 to 1.7 atoms/nm² and shows a good linear relationship versus Ir loading (green dashed line).

According to Lu et al.’s work, the larger atomic radius of metal atom inhibits its thermal diffusion and percolation into inner bulk.³⁰ All metal atoms should be anchored to the external surface. Therefore, we further calculate the Ir density by using external surface area. As shown in Table S2 and Figure 1g, the calculated Ir atom densities based on BET results (blue dashed line) display a similar linear relationship with mass loadings and are very close to the statistical data, confirming that Ir single atoms are nearly exposed on the external surface of supports and the values of Ir single-atom density are reliable. For convenience, these Ir SACs samples with different densities are designated as x -Ir₁/PC, where x represents the Ir density (atoms/nm²) in the following content.

As far as we know, such Ir SAC with P-coordination and high loading as well as surface density was rarely reported in the literature. In contrast, Ir SACs with a traditional N-coordination structure (denoted as Ir₁/NC) can only be obtained within 2 wt % by employing the same synthesis method except without addition of a phosphorous source (Figure S14). As the loading was further increased, distinct Ir nanoparticles appeared (Figure S15). This result suggests that the P-coordination strategy has an advantage in fabricating a series of Ir SACs with varying densities, which provides ideal catalysts for investigating the effect of single-atom density on the electronic structure and catalytic performance. Moreover, the electronegativity of the P atom is much smaller than that of the N atom,^{31–33} resulting in a much higher electronic density of the Ir single atom with a P-coordination structure. As shown in Figure S16a, the white-line intensity of Ir₁/PC was notably lower than that of Ir₁/NC with the same loading of 2 wt %,

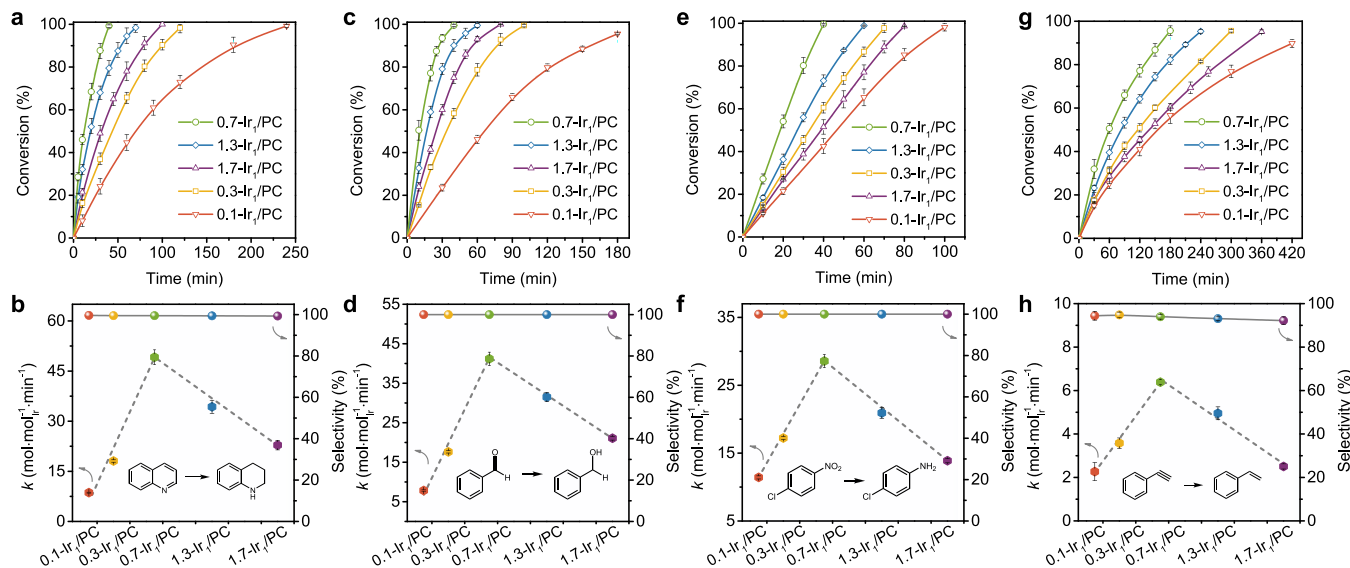


Figure 3. Catalytic hydrogenation performances of $x\text{-Ir}_1/\text{PC}$ catalysts. Time course of quinoline (a), benzaldehyde (c), *para*-chloronitrobenzene (e), and phenylacetylene (g) conversions over various $x\text{-Ir}_1/\text{PC}$ samples. Reaction rates (k) and corresponding selectivity to py-THQ (b), benzylalcohol (d), *para*-chloroaniline (f), and phenylethylene (h). The standard deviations were derived from three independent trials. Reaction conditions: substrate/catalyst_(based on Ir) = 1000, 40 mL of EtOH, 100 °C for quinoline and benzaldehyde, 60 °C for *para*-chloronitrobenzene, 2 MPa H₂; 100 °C and 0.5 MPa H₂ for phenylethylene. The selectivity was determined at the end of the run, i.e., after the complete conversion.

confirming that Ir atoms in Ir_1/PC have a much higher electronic density and higher catalytic activity (Figure S16b,c).

Atomic Structure and Chemical State Analysis. The electronic property and coordination environment of these $x\text{-Ir}_1/\text{PC}$ samples were further investigated using XAFS. The normalized Ir L₃-edge XAFS (Figure 2a) shows that the white-line intensities of $x\text{-Ir}_1/\text{PC}$ samples are between those of Ir foil and IrO₂, suggesting that Ir species are partially positively charged in these $x\text{-Ir}_1/\text{PC}$ samples. It is worth noting that with increasing Ir atom density from 0.1 to 1.7 atoms/nm², the white-line intensity displays an obvious downshift, suggesting that the newly formed adjacent Ir atoms induce the charge redistribution, which enriches the charge densities of Ir atoms gradually. The Ir 4f core-level X-ray photoelectron spectroscopy (XPS) spectra also show that the binding energy shifts downward from 61.79 to 61.21 eV (Figure 2b), consistent with the XAFS results.

The Fourier-transformed k^3 -weighted extended XAFS (FT-EXAFS) spectra demonstrate only one prominent peak at 1.78 Å (without phase-shift) corresponding to the Ir–P scattering path and the absence of Ir–Ir scattering at 2.68 Å, confirming the atomically dispersed Ir atoms in all the $x\text{-Ir}_1/\text{PC}$ samples (Figure 2c). EXAFS curves at the k space of $x\text{-Ir}_1/\text{PC}$ samples display the same shape (Figure S17). Wavelet-transformed (WT) images also show only one maximum intensity at \sim 6.5 Å⁻¹, which can be ascribed to the contribution of Ir–P coordination at the first shell (Figure 2d). Further quantitative EXAFS curve-fitting results show that the average coordination numbers (CN) of Ir in $x\text{-Ir}_1/\text{PC}$ are estimated to be \sim 4.0 with the average bond distance of Ir–P at 2.22 Å (Figure 2c and Table S3), indicating that atomically dispersed Ir species predominantly exist as $\text{Ir}_1\text{-P}_4$ configuration in all $x\text{-Ir}_1/\text{PC}$. Therefore, we can ascribe the different electronic properties of Ir species to the Ir density rather than the coordination environment in $x\text{-Ir}_1/\text{PC}$ (Figure 2e), which also provides ideal catalysts for us to investigate the effect of single-atom density on catalytic performance.

Hydrogenation Performances. We first chose selective hydrogenation of quinoline to 1,2,3,4-tetrahydroquinoline (py-THQ), an important transformation reaction in the fine chemical and pharmaceutical industry,^{34–36} as a probe reaction to systematically evaluate the catalytic performances over these $x\text{-Ir}_1/\text{PC}$ catalysts. As shown in Figure 3a, all the reaction kinetic curves display zero order when the conversions were relatively low, indicating that the hydrogenation of quinoline on these catalysts was a surface reaction because of fully exposed Ir atoms. However, notable differences of the catalytic activity can be observed under the same reaction conditions (100 °C, 2 MPa H₂, and S/C ratio of 1000). To better compare the activity difference, the reaction rates (k) are calculated and plotted as a function of Ir density (Figure 3b). Strikingly, it presents a volcano-shaped relationship. The Ir_1/PC catalyst with a moderate density of 0.7 atom/nm² shows the highest activity. The calculated apparent activation energies of $x\text{-Ir}_1/\text{PC}$ with varying densities displayed an inverse volcano relationship, consistent with the trend of activity (Figures S18 and S19). The apparent turnover frequency (TOF) and mass-specific activity for 0.7-Ir₁/PC reached as high as 3844 h⁻¹ and 421 mmol·g⁻¹·h⁻¹, respectively, which were much higher than most of reported results in the literature (Figure S20). Especially, the high mass-specific activity indicates the ability to convert the reactant over the catalyst with low mass, which is more important for industrial application.³⁷ Moreover, Ir₁/PC exhibited outstanding catalytic and structural stability after consecutive cycles (Figures S21–S23 and Table S1), suggesting the superior stability of the P-coordination structure. All these features make 0.7-Ir₁/PC an excellent hydrogenation catalyst.

We further investigated the catalytic performance of $x\text{-Ir}_1/\text{PC}$ catalysts in the selective hydrogenation of benzaldehyde, *para*-chloronitrobenzene, and phenylacetylene, three of the very important hydrogenation reactions in the fine chemical industry.^{11,20,38,39} As shown in Figure 3c–h, similar volcano relationships between activity and Ir single-atom density were

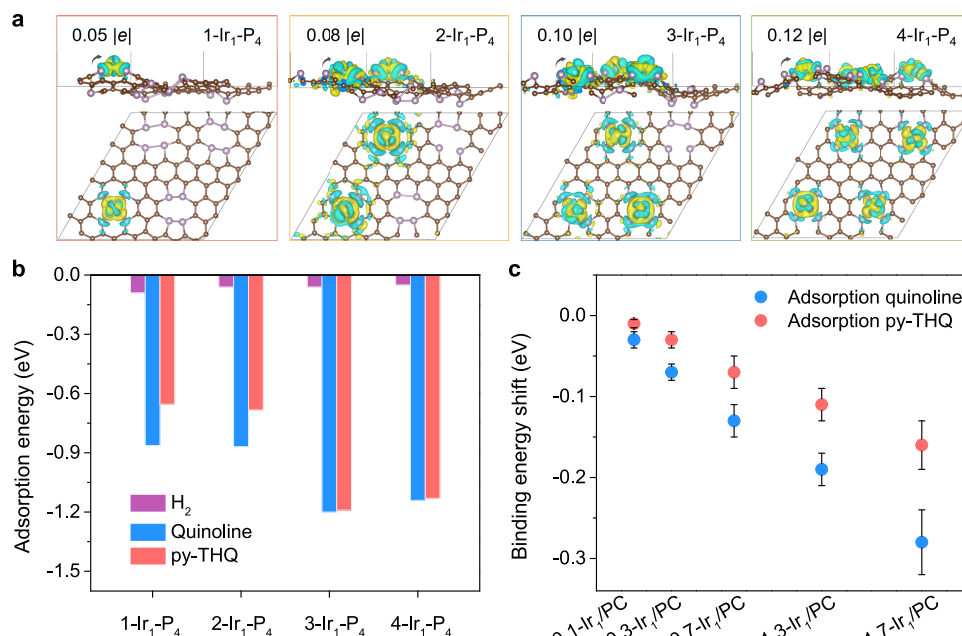


Figure 4. Theoretical analysis of electronic structure and adsorption configuration. (a) Top and side views of differential charge density of varying Ir density models. Isosurface: 0.005 e/Å⁻³. The transferred Bader charge is the average value of per Ir atom in the whole model. (b) Calculated adsorption energies of H₂, quinoline, and py-THQ. (c) Binding energy shift of x-Ir₁/PC from the XPS experiment before and after adsorption of quinoline and py-THQ.

also observed, with 0.7-Ir₁/PC being at the top. These experimental findings confirmed the presence of a volcano curve for the hydrogenation activity of x-Ir₁/PC catalysts with the same coordination structure but varying densities. As far as we know, this is the first report about the volcanic phenomena in hydrogenation reactions at the single atomic scale induced by single-atom density.

Additionally, in the selective hydrogenation of *para*-chloronitrobenzene and phenylacetylene, two more challenging reactions, the selectivity toward the desired products was maintained at or above 92%. The outstanding selectivity can be ascribed to a particular advantage of SACs of having uniform geometric and electronic structures, which allow only the target functional group to be adsorbed on the catalyst in a specific manner.¹⁹ That is, by optimizing the density of Ir single atoms, it is possible to further break the scaling relationship that is related to the activity–selectivity trade-off in chemoselective hydrogenation reactions, achieving the highest activity and selectivity simultaneously with the best 0.7-Ir₁/PC catalyst.

Furthermore, to investigate the general principle, we prepared a series of Ru₁/PC catalysts with different loadings of 0.3–6 wt % (corresponding to atom ratios in x-Ir₁/PC) using the same P-coordination strategy. As shown in Figure S24, a volcano-type relationship between Ru single-atom loading and hydrogenation activity also emerged, with a summit at a moderate loading of 2.6 wt %, which was consistent with the tendency in x-Ir₁/PC catalysts. All of these findings point to the possibility of a broad Sabatier phenomenon induced by single-atom density in hydrogenation reactions.

Mechanism Investigation. According to the above characterizations and discussions, the differences in hydrogenation activities of x-Ir₁/PC catalysts can be attributed to the intrinsic differences in electronic structures of Ir single atoms caused by density. Exploring how does the electronic state

affect the catalytic performance is therefore particularly important for the mechanistic understanding of the Sabatier phenomenon in hydrogenation reactions at the single atomic scale. Following that, density functional theory (DFT) calculations were subsequently performed to reveal the distinctive electronic structures of x-Ir₁/PC catalysts of various densities, as well as their influence on the reaction.

According to the density statistical results (Figure 1g) and atom ratios of Ir/P (Table S4), different numbers of Ir₁-P₄ single sites were evenly embedded in the same 7*7 cell of P-doped graphene for modeling (Figure S25). Within such a grid area, a maximum of four Ir₁-P₄ sites can be accommodated. The corresponding Ir density was calculated to be approximately 1.6 atoms/nm², which was quite close to the as-synthesized 1.7-Ir₁/PC sample. When the number of Ir single sites was set as 1, 2, or 3, the calculated Ir densities matched the experimental data of 0.3-Ir₁/PC, 0.7-Ir₁/PC, and 1.3-Ir₁/PC samples, respectively. After optimization, the formation energies of x-Ir₁-P₄ moieties were all below -7.2 eV, indicating the high stability of these models (Figure S25). Moreover, due to the large radius of P and Ir atoms, the configurations underwent extensive reconstruction, resulting in non-planar and asymmetric atom arrangements. As a result, these models with varying numbers of Ir₁-P₄ single sites can be employed well to represent x-Ir₁/PC catalysts with varying densities in the following theoretical calculations. It is worth mentioning that although there were residual N and abundant O atoms in all of Ir₁/PC samples (Table S4), no Ir–N/O scattering path at ~1.61 Å was observed, suggesting that these N/O atoms should be located at the second or higher coordination shell. However, it is a big challenge to identify the exact locations with current characterizations. In addition, it is well known that the activity of SACs is mainly dominated by the first-coordination shell. To facilitate the exploration of the relationship between Ir single-atom density and activity, we

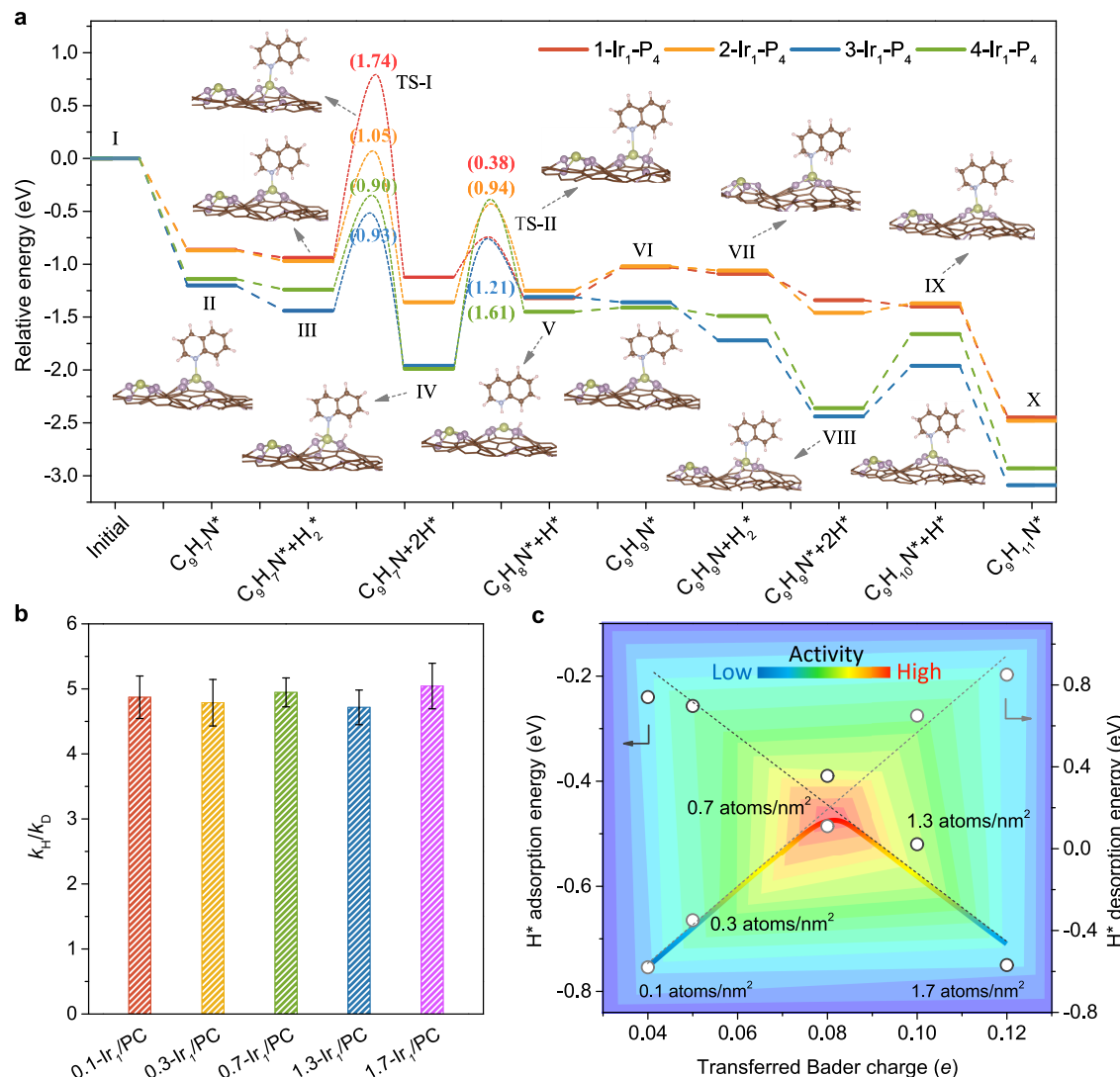


Figure 5. Theoretical calculation of reaction pathways. (a) Reaction pathways and energy profiles for quinoline hydrogenation and corresponding intermediate configurations. (b) H-D exchange results of isotope effect. (c) Sabatier relationship between transferred Bader charge and H* adsorption/desorption induced by varying Ir-density models.

thus did not consider the influence of N/O atoms in the calculation models for simplification.

The charge density difference and Bader charge were initially investigated using the optimized models. Figure 4a demonstrates electron accumulation between central Ir and P atoms, similar to other single-atom materials with P coordination in the literature.^{33,40} Moreover, when the Ir density increases, more average localized charge gathers around Ir sites, causing the Ir valence shift to metallic state, which is consistent with the XANES and XPS results (Figure 2a,b). These charge density differences indicated the interaction among these single sites in densely populated SACs through charge redistribution, resulting in different electronic structures,⁴¹ which would affect the reactant/intermediate adsorption/desorption and, consequently, catalytic performance.

For hydrogenation reactions, both H₂ dissociation and substrate activation are prerequisite. However, whether and how H₂ dissociates on isolated single metal atoms is under debate.⁴² On the one hand, the absence of a metal–metal bond in SACs results in the H₂ dissociation usually via a heterolytic pathway, which requires overcoming a larger energy barrier

than the homolytic dissociation pathway on classic metals nanoparticles. On the other hand, there is adsorption competition between the substrate and H₂ at the reaction site, especially when a single metal site is preferentially occupied by a substrate molecule with stronger affinity. Thus, we further calculated the adsorption geometries and binding energies of H₂ and quinoline molecules on Ir single atoms. In all models, it was found that quinoline was adsorbed significantly stronger than H₂ (Figure 4b and Figure S26). This finding implies that, for the catalytic reaction steps, quinoline should adsorb on Ir single atoms first. Such a process was similar to 1,3-butadiene predominantly covered on Pd single atoms during the hydrogenation reaction due to its significantly stronger affinity than H₂.²⁹ Furthermore, the calculated binding energies of py-THQ on Ir single atoms were lower than those of the quinoline reactant (Figure 4b and Figure S26), indicating that product desorption was more favorable, which was critical for preventing catalyst poisoning and ensuring smooth catalytic cycling. The XPS spectra of α -Ir₁/PC catalysts after adsorption of quinoline and py-THQ were also collected to confirm their adsorption energy

differences (Figure S27). The extent of binding energy shift indicates the adsorption strength. As shown in Figure 4c, the Ir 4f binding energy after quinoline adsorption is lower than that after py-THQ adsorption on corresponding $x\text{-Ir}_1/\text{PC}$ catalysts, which is consistent with the aforementioned theoretical results.

Based on the above results and analyses, the reaction pathways and the corresponding energy profiles over various $x\text{-Ir}_1\text{-P}_4$ models were then investigated using DFT calculations (Figure 5a, Figures S28–S30, and Table S5). It can be seen that the whole reaction process on these $x\text{-Ir}_1\text{-P}_4$ models was exothermic, indicating that the proposed reaction pathways were reasonable and thermodynamically favorable. The critical steps with major energy differences were steps III to V, where the H₂ molecule was dissociated and then hydrogenated the N=C bond of co-adsorbed quinoline, following the Langmuir–Hinshelwood (L–H) mechanism well.⁴³ Because of the stronger affinity, a quinoline molecule was adsorbed on the Ir single atom, and this process was highly exothermic by −0.86 to −1.2 eV on $x\text{-Ir}_1\text{-P}_4$ models (II). Next, a H₂ molecule was co-adsorbed and dissociated into two H atoms through the heterolytic manner at the Ir–P interface, forming Ir-H^{δ−} and P-H^{δ+} species (III–IV). This process was also found to be exothermic but with an energy barrier. The energy barrier on 1-Ir₁-P₄ was the highest (1.74 eV), which could be the consequence of the insufficient metallic state for H₂ dissolution. The activation ability of the H₂ molecule was enhanced when the Ir density was increased, and the energy barrier was gradually reduced from 1.05 to 0.90 eV. HD exchange experiments also verified that the densely packed Ir₁/PC catalyst enabled easier H₂ dissociation (Figure S31). Subsequently, the active H^{*} atom on Ir-H^{δ−} was directly transferred to the adsorbed N atom of C₉H₇N* to form C₉H₇NH* (steps IV–V). This process was exothermic at 0.2 eV, with only 0.38 eV energy barrier on 1-Ir₁-P₄. In contrast, they were endothermic on 2-Ir₁-P₄, 3-Ir₁-P₄, and 4-Ir₁-P₄, with energy barriers of 0.94, 1.21, and 1.61 eV, respectively.

Compared with the above two energy barriers, we can see that 2-Ir₁-P₄ has the lowest energy barrier (1.05 eV) in the whole reaction pathway. The activation of the H₂ molecule was the rate-determination step (RDS) on the low-density 1-Ir₁-P₄ catalyst, with the highest energy barrier of 1.74 eV. Moreover, the dissociated H^{*} atoms were adsorbed too weakly with an energy of only −0.03 eV, resulting in considerably easier desorption. In contrast, H₂ dissociation was much easier on 3-Ir₁-P₄ and 4-Ir₁-P₄ catalysts. The dissociated H^{*} atoms, on the contrary, were adsorbed substantially stronger (−0.52 and −0.75 eV), resulting in higher energy barriers for H^{*} desorption from Ir-H^{δ−} for the subsequent hydrogenation step. In other words, high-density 3-Ir₁-P₄ and 4-Ir₁-P₄ catalysts suffered too strong adsorption of reactive H^{*} atoms, resulting in the slow hydrogenation process. The adsorption and desorption of the activated H^{*} atom on the 2-Ir₁-P₄ catalyst were moderate, that is, neither too weak nor too strong, resulting in the highest activity. A similar trend was also observed in the activation of the second H₂ molecule and subsequent hydrogenation process during the VII to IX steps. In addition, H₂/D₂ kinetic isotope effect (KIE) experimental results (Figure 5b and Figure S32) show large values of $k_{\text{H}}/k_{\text{D}}$ exceeding 4.5 for all catalysts, confirming that the RDS involves H₂ heterolytic dissociation or H^{*} atom transfer, which is consistent very well with DFT calculation results and the reported H₂ dissociation manner on other SACs in the literature.^{33,44,45}

Therefore, the Sabatier phenomenon in above hydrogenation reactions over various $x\text{-Ir}_1/\text{PC}$ catalysts with varying densities should be triggered by the trade-off relation between the adsorption and desorption strength of the activated H^{*} atoms intermediate on Ir single atoms. Finally, we found a well-matched volcano relationship when we plotted the transferred Bader charge vs H^{*} adsorption and desorption energies on $x\text{-Ir}_1\text{-P}_4$ models (Figure 5c and Figure S33). 0.1-Ir₁/PC and 0.3-Ir₁/PC catalysts with lower transferred Bader charge were located on the left side of the Sabatier plot. Their catalytic activity was mainly limited by a too weak adsorption. In contrast, 1.3-Ir₁/PC and 1.7-Ir₁/PC catalysts with higher densities and more transferred Bader charges were found on the right side, in which the catalytic activities were mainly restricted by the too strong desorption energy. The 0.7-Ir₁/PC catalyst with a modest transferred Bader charge was at the top, with the optimum adsorption–desorption equilibrium strength. The transferred Bader charge was usually recognized as a key factor to influence the electronic structure and activity of catalysts in many catalytic reactions.^{46–49} Thus, we proposed that it was also a suitable descriptor to interpret the Sabatier phenomenon in our reaction system.

It is well known that the electronic structure of active centers influences the adsorption and activation of reactants and, consequently, catalytic performance. For hydrogenation reactions, the absence of a metal–metal bond in SACs usually results in the H₂ dissociation via a heterolytic pathway to form H^{δ−} and H^{δ+}, which are subsequently transferred for hydrogenation. Therefore, the H^{*} adsorption/desorption energies should be the key factor for the catalytic performance, which is in turn related to the electronic structure of metal single atoms.

CONCLUSIONS

In summary, we observed a new Sabatier phenomenon in hydrogenation reactions at the single atomic scale with a series of Ir SACs of varying densities. Experimental and DFT calculation results disclosed that the adsorption and desorption strength of the activated H^{*} atoms on Ir single atoms was a key factor for the Sabatier phenomenon. Different from a great number of studies focusing on the regulation coordination environments of SACs,^{40,45,50} this work emphasizes how the single-atom density affects the electronic structures of central metal atoms and their catalytic performances in hydrogenation reactions. We notice that the neighboring single sites could indeed work in synergy to further enhance the reactivity of SACs in various reactions in recent publications.^{26,30,51} However, the mechanism behind such effects was different in various reactions. The fundamental investigation into the Sabatier principle at the atomic scale in hydrogenation reactions induced by single-atom density in this work can guide the future design of more efficient and practicable SACs for a variety of catalytic reactions.

ASSOCIATED CONTENT

Supporting Information

The Supporting Information is available free of charge at <https://pubs.acs.org/doi/10.1021/jacs.3c00786>.

Experimental details, supported structure characterizations, and catalytic analysis (PDF)

AUTHOR INFORMATION

Corresponding Authors

Xiaohu Yu — Institute of Theoretical and Computational Chemistry, Shaanxi Key Laboratory of Catalysis, School of Chemical & Environment Sciences, Shaanxi University of Technology, Hanzhong 723000, China; orcid.org/0000-0003-3670-2859; Email: yuxiaohu@sut.edu.cn

Ding Ma — Beijing National Laboratory for Molecular Sciences, New Cornerstone Science Laboratory, College of Chemistry and Molecular Engineering, Peking University, Beijing 100871, China; orcid.org/0000-0002-3341-2998; Email: dma@pku.edu.cn

Changyan Cao — Beijing National Laboratory for Molecular Sciences, CAS Key Laboratory of Molecular Nanostructure and Nanotechnology, CAS Research/Education Center for Excellence in Molecular Sciences, Institute of Chemistry, Chinese Academy of Sciences, Beijing 100190, China; University of the Chinese Academy of Sciences, Beijing 100049, China; orcid.org/0000-0003-2139-1648; Email: cyc@iccas.ac.cn

Authors

Hongqiang Jin — Beijing National Laboratory for Molecular Sciences, CAS Key Laboratory of Molecular Nanostructure and Nanotechnology, CAS Research/Education Center for Excellence in Molecular Sciences, Institute of Chemistry, Chinese Academy of Sciences, Beijing 100190, China; University of the Chinese Academy of Sciences, Beijing 100049, China

Runqing Zhao — Beijing National Laboratory for Molecular Sciences, CAS Key Laboratory of Molecular Nanostructure and Nanotechnology, CAS Research/Education Center for Excellence in Molecular Sciences, Institute of Chemistry, Chinese Academy of Sciences, Beijing 100190, China; University of the Chinese Academy of Sciences, Beijing 100049, China

Peixin Cui — Key Laboratory of Soil Environment and Pollution Remediation, Institute of Soil Science, Chinese Academy of Sciences, Nanjing 210008, China; orcid.org/0000-0002-9887-2784

Xiaolong Liu — Beijing National Laboratory for Molecular Sciences, CAS Key Laboratory of Molecular Nanostructure and Nanotechnology, CAS Research/Education Center for Excellence in Molecular Sciences, Institute of Chemistry, Chinese Academy of Sciences, Beijing 100190, China; University of the Chinese Academy of Sciences, Beijing 100049, China

Jie Yan — Beijing National Laboratory for Molecular Sciences, New Cornerstone Science Laboratory, College of Chemistry and Molecular Engineering, Peking University, Beijing 100871, China

Weiguo Song — Beijing National Laboratory for Molecular Sciences, CAS Key Laboratory of Molecular Nanostructure and Nanotechnology, CAS Research/Education Center for Excellence in Molecular Sciences, Institute of Chemistry, Chinese Academy of Sciences, Beijing 100190, China; University of the Chinese Academy of Sciences, Beijing 100049, China; orcid.org/0000-0001-5390-6787

Complete contact information is available at:

<https://pubs.acs.org/10.1021/jacs.3c00786>

Author Contributions

#H.J. and R.Z. contributed equally to this work.

Author Contributions

The manuscript was written through contributions of all authors. All authors have given approval to the final version of the manuscript.

Notes

The authors declare no competing financial interest.

ACKNOWLEDGMENTS

We thank the National Key R&D Program of China (grant nos. 2018YFA0208504 and 2018YFA0703503), the National Natural Science Foundation of China (NSFC 22272181, 92161112, 21932006, and 22273053), the Youth Innovation Promotion Association of CAS (Y2017049), and National Science Basic Research Program of Shaanxi (no. S2020-JC-WT-0001) for financial support. We also thank Prof. Jun Li from Tsinghua University for his helpful discussions about DFT calculations. This paper is dedicated to Prof. Jun Li on the occasion of his 60th birthday.

REFERENCES

- (1) Stamenkovic, V.; Mun, B. S.; Mayrhofer, K. J.; Ross, P. N.; Markovic, N. M.; Rossmeisl, J.; Greeley, J.; Norskov, J. K. Changing the activity of electrocatalysts for oxygen reduction by tuning the surface electronic structure. *Angew. Chem., Int. Ed.* **2006**, *45*, 2897–2901.
- (2) Medford, A. J.; Vojvodic, A.; Hummelshøj, J. S.; Voss, J.; Abild-Pedersen, F.; Studt, F.; Bligaard, T.; Nilsson, A.; Nørskov, J. K. From the Sabatier principle to a predictive theory of transition-metal heterogeneous catalysis. *J. Catal.* **2015**, *328*, 36–42.
- (3) Hu, S.; Li, W. X. Sabatier principle of metal-support interaction for design of ultrastable metal nanocatalysts. *Science* **2021**, *374*, 1360–1365.
- (4) Vogt, C.; Weckhuysen, B. M. The concept of active site in heterogeneous catalysis. *Nat. Rev. Chem.* **2022**, *6*, 89–111.
- (5) Sun, G.; Zhao, Z. J.; Mu, R.; Zha, S.; Li, L.; Chen, S.; Zang, K.; Luo, J.; Li, Z.; Purdy, S. C.; Kropf, A. J.; Miller, J. T.; Zeng, L.; Gong, J. Breaking the scaling relationship via thermally stable Pt/Cu single atom alloys for catalytic dehydrogenation. *Nat. Commun.* **2018**, *9*, 4454.
- (6) Pérez-Ramirez, J.; López, N. Strategies to break linear scaling relationships. *Nat. Catal.* **2019**, *2*, 971–976.
- (7) Wang, L.; Diao, J.; Peng, M.; Chen, Y.; Cai, X.; Deng, Y.; Huang, F.; Qin, X.; Xiao, D.; Jiang, Z.; Wang, N.; Sun, T.; Wen, X.; Liu, H.; Ma, D. Cooperative sites in fully exposed Pd clusters for low-temperature direct dehydrogenation reaction. *ACS Catal.* **2021**, *11*, 11469–11477.
- (8) Vogt, C.; Groeneveld, E.; Kamsma, G.; Nachtegaal, M.; Lu, L.; Kiely, C. J.; Berben, P. H.; Meirer, F.; Weckhuysen, B. M. Unravelling structure sensitivity in CO₂ hydrogenation over nickel. *Nat. Catal.* **2018**, *1*, 127–134.
- (9) Xiao, M.; Chen, Y.; Zhu, J.; Zhang, H.; Zhao, X.; Gao, L.; Wang, X.; Zhao, J.; Ge, J.; Jiang, Z.; Chen, S.; Liu, C.; Xing, W. Climbing the apex of the ORR volcano plot via binuclear site construction: electronic and geometric engineering. *J. Am. Chem. Soc.* **2019**, *141*, 17763–17770.
- (10) Xin, H.; Vojvodic, A.; Voss, J.; Nørskov, J. K.; Abild-Pedersen, F. Effects of d-band shape on the surface reactivity of transition-metal alloys. *Phys. Rev. B* **2014**, *89*, 1–5.
- (11) Guan, Q.; Zhu, C.; Lin, Y.; Vovk, E. I.; Zhou, X.; Yang, Y.; Yu, H.; Cao, L.; Wang, H.; Zhang, X.; Liu, X.; Zhang, M.; Wei, S.; Li, W.-X.; Lu, J. Bimetallic monolayer catalyst breaks the activity–selectivity trade-off on metal particle size for efficient chemoselective hydrogénations. *Nat. Catal.* **2021**, *4*, 840–849.
- (12) Yang, Y.; Zhu, X.; Wang, L.; Lang, J.; Yao, G.; Qin, T.; Ren, Z.; Chen, L.; Liu, X.; Li, W.; Wan, Y. Breaking scaling relationships in alkynol semi-hydrogenation by manipulating interstitial atoms in Pd with d-electron gain. *Nat. Commun.* **2022**, *13*, 2754.

- (13) Calle-Vallejo, F.; Martinez, J. I.; Garcia-Lastra, J. M.; Rossmeisl, J.; Koper, M. T. Physical and chemical nature of the scaling relations between adsorption energies of atoms on metal surfaces. *Phys. Rev. Lett.* **2012**, *108*, No. 116103.
- (14) Liu, K.; Jiang, L.; Huang, W.; Zhu, G.; Zhang, Y. J.; Xu, C.; Qin, R.; Liu, P.; Hu, C.; Wang, J.; Li, J. F.; Yang, F.; Fu, G.; Zheng, N. Atomic overlayer of permeable microporous cuprous oxide on palladium promotes hydrogenation catalysis. *Nat. Commun.* **2022**, *13*, 2597.
- (15) Wang, A.; Li, J.; Zhang, T. Heterogeneous single-atom catalysis. *Nat. Rev. Chem.* **2018**, *2*, 65–81.
- (16) Wang, H.; Gu, X. K.; Zheng, X.; Pan, H.; Zhu, J.; Chen, S.; Cao, L.; Li, W. X.; Lu, J. Disentangling the size-dependent geometric and electronic effects of palladium nanocatalysts beyond selectivity. *Sci. Adv.* **2019**, *5*, No. eaat6413.
- (17) Chu, C.; Huang, D.; Gupta, S.; Weon, S.; Niu, J.; Stavitski, E.; Muhich, C.; Kim, J. H. Neighboring Pd single atoms surpass isolated single atoms for selective hydrodehalogenation catalysis. *Nat. Commun.* **2021**, *12*, 5179.
- (18) Liu, L.; Corma, A. Metal catalysts for heterogeneous catalysis: from single atoms to nanoclusters and nanoparticles. *Chem. Rev.* **2018**, *118*, 4981–5079.
- (19) Zhang, L.; Zhou, M.; Wang, A.; Zhang, T. Selective hydrogenation over supported metal catalysts: from nanoparticles to single atoms. *Chem. Rev.* **2020**, *120*, 683–733.
- (20) Westerhaus, F. A.; Jagadeesh, R. V.; Wienhoefer, G.; Pohl, M.-M.; Radnik, J.; Surkus, A.-E.; Rabeha, J.; Junge, K.; Junge, H.; Nielsen, M.; Brueckner, A.; Beller, M. Heterogenized cobalt oxide catalysts for nitroarene reduction by pyrolysis of molecularly defined complexes. *Nat. Chem.* **2013**, *5*, 537–543.
- (21) Wei, H.; Liu, X.; Wang, A.; Zhang, L.; Qiao, B.; Yang, X.; Huang, Y.; Miao, S.; Liu, J.; Zhang, T. FeO_x-supported platinum single-atom and pseudo-single-atom catalysts for chemoselective hydrogenation of functionalized nitroarenes. *Nat. Commun.* **2014**, *5*, 6634.
- (22) Zhou, P.; Jiang, L.; Wang, F.; Deng, K.; Lv, K.; Zhang, Z. High performance of a cobalt-nitrogen complex for the reduction and reductive coupling of nitro compounds into amines and their derivatives. *Sci. Adv.* **2017**, *3*, No. e1601945.
- (23) Lang, R.; Du, X.; Huang, Y.; Jiang, X.; Zhang, Q.; Guo, Y.; Liu, K.; Qiao, B.; Wang, A.; Zhang, T. Single-atom catalysts based on the metal-oxide interaction. *Chem. Rev.* **2020**, *120*, 11986–12043.
- (24) Li, Z.; Ji, S.; Liu, Y.; Cao, X.; Tian, S.; Chen, Y.; Niu, Z.; Li, Y. Well-defined materials for heterogeneous catalysis: from nanoparticles to isolated single-atom sites. *Chem. Rev.* **2020**, *120*, 623–682.
- (25) He, X.; Zhang, H.; Zhang, X.; Zhang, Y.; He, Q.; Chen, H.; Cheng, Y.; Peng, M.; Qin, X.; Ji, H.; Ma, D. Building up libraries and production line for single atom catalysts with precursor-atomization strategy. *Nat. Commun.* **2022**, *13*, 5721.
- (26) Jin, Z.; Li, P.; Meng, Y.; Fang, Z.; Xiao, D.; Yu, G. Understanding the inter-site distance effect in single-atom catalysts for oxygen electroreduction. *Nat. Catal.* **2021**, *4*, 615–622.
- (27) Wang, B.; Cheng, C.; Jin, M.; He, J.; Zhang, H.; Ren, W.; Li, J.; Wang, D.; Li, Y. A Site Distance Effect Induced by Reactant Molecule Matchup in Single-Atom Catalysts for Fenton-Like Reactions. *Angew. Chem., Int. Ed.* **2022**, *61*, No. e202207268.
- (28) Yao, D.; Tang, C.; Zhi, X.; Johannessen, B.; Slattery, A.; Chern, S.; Qiao, S. Z. Inter-Metal Interaction with a Threshold Effect in NiCu Dual-Atom Catalysts for CO₂ Electroreduction. *Adv. Mater.* **2023**, *35*, No. e2209386.
- (29) Song, J.; Chen, Z.; Cai, X.; Zhou, X.; Zhan, G.; Li, R.; Wei, P.; Yan, N.; Xi, S.; Loh, K. P. Promoting Dinuclear-Type Catalysis in Cu₁–C₃N₄ Single-Atom Catalysts. *Adv. Mater.* **2022**, *34*, No. e2204638.
- (30) Hai, X.; Xi, S.; Mitchell, S.; Harrath, K.; Xu, H.; Akl, D. F.; Kong, D.; Li, J.; Li, Z.; Sun, T.; Yang, H.; Cui, Y.; Su, C.; Zhao, X.; Li, J.; Perez-Ramirez, J.; Lu, J. Scalable two-step annealing method for preparing ultra-high-density single-atom catalyst libraries. *Nat. Nanotechnol.* **2022**, *17*, 174–181.
- (31) Yuan, K.; Luetzenkirchen-Hecht, D.; Li, L.; Shuai, L.; Li, Y.; Cao, R.; Qiu, M.; Zhuang, X.; Leung, M. K. H.; Chen, Y.; Scherf, U. Boosting oxygen reduction of single iron active sites via geometric and electronic engineering: nitrogen and phosphorus dual coordination. *J. Am. Chem. Soc.* **2020**, *142*, 2404–2412.
- (32) Wan, J.; Zhao, Z.; Shang, H.; Peng, B.; Chen, W.; Pei, J.; Zheng, L.; Dong, J.; Cao, R.; Sarangi, R.; Jiang, Z.; Zhou, D.; Zhuang, Z.; Zhang, J.; Wang, D.; Li, Y. In situ phosphatizing of triphenylphosphine encapsulated within metal-organic frameworks to design atomic Co₁P₁N₃ interfacial structure for promoting catalytic performance. *J. Am. Chem. Soc.* **2020**, *142*, 8431–8439.
- (33) Jin, H.; Li, P.; Cui, P.; Shi, J.; Zhou, W.; Yu, X.; Song, W.; Cao, C. Unprecedentedly high activity and selectivity for hydrogenation of nitroarenes with single atomic Co₁N₃P₁ sites. *Nat. Commun.* **2022**, *13*, 723.
- (34) Muthukrishnan, I.; Sridharan, V.; Menendez, J. C. Progress in the chemistry of tetrahydroquinolines. *Chem. Rev.* **2019**, *119*, 5057–5191.
- (35) Li, S.; Cao, R.; Xu, M.; Deng, Y.; Lin, L.; Yao, S.; Liang, X.; Peng, M.; Gao, Z.; Ge, Y.; Liu, J. X.; Li, W. X.; Zhou, W.; Ma, D. Atomically dispersed Ir/α-MoC catalyst with high metal loading and thermal stability for water-promoted hydrogenation reaction. *Natl. Sci. Rev.* **2022**, *9*, No. nwab026.
- (36) Wang, X.; Chen, W.; Zhang, L.; Yao, T.; Liu, W.; Lin, Y.; Ju, H.; Dong, J.; Zheng, L.; Yan, W.; Zheng, X.; Li, Z.; Wang, X.; Yang, J.; He, D.; Wang, Y.; Deng, Z.; Wu, Y.; Li, Y. Uncoordinated amine groups of metal-organic frameworks to anchor single Ru sites as chemoselective catalysts toward the hydrogenation of quinoline. *J. Am. Chem. Soc.* **2017**, *139*, 9419–9422.
- (37) Zhang, X.; Zhang, M.; Deng, Y.; Xu, M.; Artiglia, L.; Wen, W.; Gao, R.; Chen, B.; Yao, S.; Zhang, X.; Peng, M.; Yan, J.; Li, A.; Jiang, Z.; Gao, X.; Cao, S.; Yang, C.; Kropf, A. J.; Shi, J.; Xie, J.; Bi, M.; van Bokhoven, J. A.; Li, Y. W.; Wen, X.; Flytzani-Stephanopoulos, M.; Shi, C.; Zhou, W.; Ma, D. A stable low-temperature H₂-production catalyst by crowding Pt on α-MoC. *Nature* **2021**, *589*, 396–401.
- (38) Jagadeesh, R. V.; Surkus, A.-E.; Junge, H.; Pohl, M.-M.; Radnik, J.; Rabeha, J.; Huan, H.; Schuenemann, V.; Brueckner, A.; Beller, M. Nanoscale Fe₂O₃-based catalysts for selective hydrogenation of nitroarenes to anilines. *Science* **2013**, *342*, 1073–1076.
- (39) Lin, L.; Yao, S.; Gao, R.; Liang, X.; Yu, Q.; Deng, Y.; Liu, J.; Peng, M.; Jiang, Z.; Li, S.; Li, Y. W.; Wen, X. D.; Zhou, W.; Ma, D. A highly CO-tolerant atomically dispersed Pt catalyst for chemoselective hydrogenation. *Nat. Nanotechnol.* **2019**, *14*, 354–361.
- (40) Sun, X.; Sun, L.; Li, G.; Tuo, Y.; Ye, C.; Yang, J.; Low, J.; Yu, X.; Bitter, J. H.; Lei, Y.; Wang, D.; Li, Y. Phosphorus tailors the d-band center of copper atomic sites for efficient CO₂ photoreduction under visible-light irradiation. *Angew. Chem., Int. Ed.* **2022**, *61*, No. e202207677.
- (41) Jin, H.; Cui, P.; Cao, C.; Yu, X.; Zhao, R.; Ma, D.; Song, W. Understanding the Density-Dependent Activity of Cu Single-Atom Catalyst in the Benzene Hydroxylation Reaction. *ACS Catal.* **2023**, *13*, 1316–1325.
- (42) Yan, H.; Lv, H.; Yi, H.; Liu, W.; Xia, Y.; Huang, X.; Huang, W.; Wei, S.; Wu, X.; Lu, J. Understanding the underlying mechanism of improved selectivity in Pd₁ single-atom catalyzed hydrogenation reaction. *J. Catal.* **2018**, *366*, 70–79.
- (43) Yu, I. K. M.; Deng, F.; Chen, X.; Cheng, G.; Liu, Y.; Zhang, W.; Lercher, J. A. Impact of hydronium ions on the Pd-catalyzed furfural hydrogenation. *Nat. Commun.* **2022**, *13*, 7154.
- (44) Liu, P.; Zhao, Y.; Qin, R.; Mo, S.; Chen, G.; Gu, L.; Chevrier, D. M.; Zhang, P.; Guo, Q.; Zang, D.; Wu, B.; Fu, G.; Zheng, N. Photochemical route for synthesizing atomically dispersed palladium catalysts. *Science* **2016**, *352*, 797–800.
- (45) Li, M.; Zhang, C.; Tang, Y.; Chen, Q.; Li, W.; Han, Z.; Chen, S.; Lv, C.; Yan, Y.; Zhang, Y.; Zheng, W.; Wang, P.; Guo, X.; Ding, W. Environment molecules boost the chemoselective hydrogenation of nitroarenes on cobalt single-atom catalysts. *ACS Catal.* **2022**, *12*, 11960–11973.

(46) Woodcox, M.; Young, J.; Smeu, M. *Ab initio* investigation of the elastic properties of bismuth-based alloys. *Phys. Rev. B* **2019**, *100*, 1–8.

(47) Li, A.; Kong, S.; Guo, C.; Ooka, H.; Adachi, K.; Hashizume, D.; Jiang, Q.; Han, H.; Xiao, J.; Nakamura, R. Enhancing the stability of cobalt spinel oxide towards sustainable oxygen evolution in acid. *Nat. Catal.* **2022**, *5*, 109–118.

(48) Niu, H.; Wang, X.; Shao, C.; Liu, Y.; Zhang, Z.; Guo, Y. Revealing the oxygen reduction reaction activity origin of single atoms supported on g-C₃N₄ monolayers: a first-principles study. *J. Mater. Chem. A* **2020**, *8*, 6555–6563.

(49) Deng, Y.; Guo, Y.; Jia, Z.; Liu, J. C.; Guo, J.; Cai, X.; Dong, C.; Wang, M.; Li, C.; Diao, J.; Jiang, Z.; Xie, J.; Wang, N.; Xiao, H.; Xu, B.; Zhang, H.; Liu, H.; Li, J.; Ma, D. Few-atom Pt ensembles enable efficient catalytic cyclohexane dehydrogenation for hydrogen production. *J. Am. Chem. Soc.* **2022**, *144*, 3535–3542.

(50) Wang, L.; Zhu, C.; Xu, M.; Zhao, C.; Gu, J.; Cao, L.; Zhang, X.; Sun, Z.; Wei, S.; Zhou, W.; Li, W. X.; Lu, J. Boosting activity and stability of metal single-atom catalysts via regulation of coordination number and local composition. *J. Am. Chem. Soc.* **2021**, *143*, 18854–18858.

(51) Li, H.; Wang, L.; Dai, Y.; Pu, Z.; Lao, Z.; Chen, Y.; Wang, M.; Zheng, X.; Zhu, J.; Zhang, W.; Si, R.; Ma, C.; Zeng, J. Synergetic interaction between neighbouring platinum monomers in CO₂ hydrogenation. *Nat. Nanotechnol.* **2018**, *13*, 411–417.